# Solar chimney power plant integrated with a photocatalytic reactor to remove atmospheric methane: A numerical analysis

Tingzhen Ming [a,b], Haoyu Gui [a], Tianhao Shi [a], Hanbing Xiong [a], Yongjia Wu [a,*], Yimin Shao [c], Wei Li [c,*], Xiaohua Lu [d], Renaud de Richter [e]

[a] School of Civil Engineering and Architecture, Wuhan University of Technology No.122 Luoshi Road, Hongshan District, Wuhan 430070, China
[b] School of Architectural Engineering, Huanggang Normal University No. 146 Xingang Second Road, Huanggang 438000, China
[c] Institute for Materials and Processes, School of Engineering, The University of Edinburgh, Edinburgh EH9 3FB, Scotland, UK
[d] College of Chemical Engineering, State Key Laboratory of Materials-oriented Chemical Engineering, Nanjing Tech University, Nanjing 211816, China
[e] Tour-Solaire.Fr, 8 Impasse des Papillons, F34090 Montpellier, France

ARTICLE INFO

ABSTRACT

Methane ($CH_4$) is the second largest contributor to global warming among all greenhouses gases. A solar chimney power plant integrated with a photocatalytic reactor (SCPP-PCR) is a promising large-scale method for removing $CH_4$ from the atmosphere. This study used computational fluid dynamics (CFD) to investigate the performance and factors influencing photocatalytic oxidation of methane by the SCPP-PCR system. The geometry of a SCPP is the same as the prototype of the SCPP built in Manzanares (Spain). The PCR is designed based on a honeycomb monolith photoreactor. The numerical results revealed that the SCPP-PCR system can degraded 21,312 g methane per day with the actual solar radiation data when the channel diameter of the honeycomb PCR was 4 mm and channel length was 8 m. Although increasing the length or decreasing the channel diameter of the PCR would improve photocatalytic efficiency, the rate of airflow of the system would be reduced. The maximum methane purification rate of the SCPP-PCR system was determined.

## 1. Introduction

The "21st United Nations Climate Change Conference" held in Paris in December 2015 agreed to a global response to climate change after 2020. The Paris Agreement aimed to control the rise in average global temperature 1.5–2 °C lower than the pre-industrial level. This is an ambitious task requiring a rapid decrease in greenhouse gas (GHG) emissions. However, in some sectors, e.g., agriculture and aviation, it is difficult to eliminate GHG emissions entirely. We must develop technologies to remove GHGs from the atmosphere on a large scale (The Royal Society, 2018).

$CO_2$ is the most significant contributor to global warming among all GHGs. Thus, it is the primary focus of most GHG removal research. To date, little attention has been given to the removal of atmospheric non-$CO_2$ GHGs (Jackson et al., 2019). The global warming potential (GWP) is a measure of the potency of a GHG. Many non-$CO_2$ atmospheric gases have a high GWP. For example, methane ($CH_4$) has a 27–35 times higher GWP than $CO_2$ over 100 years which represents almost 25% of the radiative forcing of long-lived (lifetime $\geq$ 10 years) GHGs.

The technology of semiconductor photocatalysis (PC) has shown broad prospects in the field of GHG conversion and pollutant degradation in recent years (Li et al., 2019; Xiang et al., 2012; Chen et al., 2012). Mohamedali et al. (2020) proposed converting methane to oxygenated hydrocarbons or syngas as an attractive way to mitigate the greenhouse effect. Krishna et al. (2004) used uranyl-anchored MCM-41 as a heterogeneous photocatalyst to confirm the high activity of total oxidation of methane to carbon dioxide at room temperature under sunlight. In et al. (2011) investigated the photocatalytic performance of methane decomposition over vertically aligned $TiO_2$ nanotube arrays. According to the experimental results, the optimal thickness of the photocatalyst for methane oxidation was about 575 nm under 367-nm illumination. Chen et al. (2016) provided a two-step photocatalytic reaction process to explain the photocatalytic oxidation of methane. Temperature fluctuations had little effect on methane photo-oxidation, and the reaction process proceeded faster at lower methane concentrations, demonstrating the prospects of photocatalytic oxidation for atmospheric methane degradation. In general, most methane PS research is in the laboratory stage. Only a few studies have been conducted outdoors due to numerous uncontrollable factors in the outdoor photocatalysis

**Nomenclature**

| | |
|---|---|
| $a$ | Thermal diffusivity ($m^2/s$) |
| $B, B_1, B_2$ | Constants for measured experimentally |
| $C_{1\varepsilon}, C_{2\varepsilon}, C_{3\varepsilon}$ | Constants for turbulent model |
| $C$ | Inertia coefficient |
| $c_1$ | Mole concentration of Methane ($mol/m^3$) |
| $c_2$ | Mole concentration of Oxygen ($mol/m^3$) |
| $c_p$ | Specific heat at constant pressure ($J/(kg\ K)$) |
| $D_P$ | Pore diameter of porous media (i.e. channel diameter of honeycomb monolith PCR) ($mm$) |
| $E_s$ | Photocatalytic efficiency |
| $g$ | Acceleration of gravity ($m/s^2$) |
| $G$ | Solar radiation intensity ($W/m^2$) |
| $G_k$ | Turbulence kinetic energy generation due to the mean velocity gradients ($J$) |
| $G_b$ | Turbulence kinetic energy generation due to turbulence ($J$) |
| $H$ | Collector height ($m$) |
| $\overrightarrow{J_i}$ | Diffusion flux of species $i$ ($mol/(s{\cdot}m^3)$) |
| $J_1$ | Mole fraction of Methane at system entrance ($ppb$) |
| $J_2$ | Mole fraction of Methane at system exit ($ppb$) |
| $K$ | Permeability |
| $L$ | Length of PCR (i.e. channel length of honeycomb monolith) ($m$) |
| $p$ | pressure ($Pa$) |
| $q$ | Heat flux through the ground underneath the collector ($W/m^2$) |
| $Ra$ | Rayleigh number |
| $R_m$ | Volume reaction rate of methane photocatalysis ($mol{\cdot}m^{-3}s^{-1}$) |
| $R_p$ | Purification rate ($g/s$) |
| $r_{AI}$ | Reaction rate per absorbed irradiation intensity and unit of catalyst surface ($mol{\cdot}W^{-1}s^{-1}$) |
| $S$ | Surface area of porous media zone ($m^2$) |
| $S_\Phi$ | Momentum loss term |
| $S_i$ | Extra rate due to the discrete phase |
| $SSA$ | Specific surface area ($m^2$) |
| $t$ | Time ($s$) |
| $T$ | Temperature ($K$) |
| $T_0$ | Ambient temperature ($K$) |
| $u$ | Average velocity magnitude in the axial direction ($m/s$) |
| $V$ | Apparent volume of porous media zone ($m^3$) |
| $x, y, z$ | Cartesian space coordinates |

*Greek symbols*

| | |
|---|---|
| $v$ | Kinetic viscosity ($m^2/s$) |
| $\beta$ | Volume coefficient of expansion ($1/K$) |
| $\rho$ | Air density ($kg/m^3$) |
| $\tau$ | Shear stress caused by viscosity ($N/m^2$) |
| $k$ | Karman constant |
| $\gamma$ | Porosity |

process. Some $NO_x$ outdoor photocatalytic experiments can be found in the literature (Guerrini, 2012; Gallus et al., 2015).

Methane is photocatalytically transformed into water vapor and $CO_2$, and the potency of the GHGs is significantly lower than the precursor (Yuliati and Yoshida, 2008).

$$CH_4 + 2O_2 \rightarrow 2H_2O + CO_2;$$
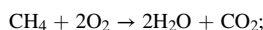
This PC process allows for harnessing sunlight to promote the destruction of $CH_4$, and has been proven very effective on a laboratory scale (Chen et al., 2016). However, process intensification is needed for methane removal at a climatically relevant scale, which requires sufficient airflow given the extreme dilution of methane. Significant airflow must be collected, processed under well-controlled parameters (i.e., light intensity, wind speed and direction, and relative humidity), and monitored in-situ.

de Richter et al. first proposed a novel technology of combining a solar chimney power plant (SCPP) with PC (de_Richter et al., 2017). This is an emerging technology for non-$CO_2$ GHG removal discovered in two of the latest reports from the Intergovernmental Panel on Climate Change (IPCC, 2018) and the Royal Society (The Royal Society, 2018).

The idea of the SCPP was proposed by Schlaich in 1978, and the first 50 kW SCPP prototype was built and successfully operated in Manzanares, Spain in the 1980s, also known as the Manzanares pilot plant (HAAF et al., 1983). Subsequently, a growing number of researchers engaged in SCPP research, and the development of this technology was summarized in several reviews (Guo et al., 2019; Zhou and Xu, 2016; Ming et al., 2017; Kasaeian et al., 2017). A conventional SCPP utilizes the updraft produced by the buoyancy effect to generate electricity. It mainly consists of four essential parts: the collector, the chimney, the energy storage layer, and the turbine. A comprehensive analysis of SCPPs is provided by Bernardes et al. (2003). They described the flow and heat transfer characteristics of an SCPP, and estimated the system power output. Maia et al. (2009) analyzed the effects of geometric parameters and the physical properties of the materials on the solar chimney. They found that the tower dimensions were the most

significant physical variables to optimize the performance of the SCPP system. Later, Ming et al. (2013) discussed the effect of chimney shape on SCPP performance. The influence of the cylindrical chimney tower dimensions on overall system performance was furtherly studied. Guo et al. (2016) proposed an analytical approach to evaluate the optimal turbine pressure drop ratio. They discussed the influence of solar radiation and ambient temperature on the optimal turbine pressure drop ratio.

SCPP technology is a large-scale renewable energy power generating technology that utilizes the large-scale solar energy resource and produces a large amount of airflow. When solar irradiation intensity and turbine rotational speed are 800 $W/m^2$ and 100 r/min, respectively, the 50 kW Manzanares pilot plant provides about 700 $m^3/s$ airflow. A 200 MW commercial SCPP provides airflow > 20,000 $m^3/s$. However, due to the low energy conversion efficiency of an SCPP, some innovative SCPP hybrid systems have aroused the interest of researchers. These novel SCPP systems have been applied in various fields, including freshwater generation from air (Ming et al., 2016; Wu et al., 2020), alleviating the problem of urban air pollution (Zhou et al., 2015; Gong et al., 2017; Cao et al., 2018), desalination of seawater with a modified SCPP (Zuo et al., 2018; Liu et al., 2020), and improving the partial climate (Zhou et al., 2008; Ming et al., 2014).

The SCPP-PC is proposed using SCPPs to generate the necessary mass airflow driven only by solar energy (de_Richter et al., 2013). Fig. 1 illustrates the operating principle of the SCPP-photocatalytic reactor (PCR) system. The SCPP is comprised of a high chimney at the center of a large solar collector. Strong airflow is generated in the chimney by the buoyance force caused by the heated air under the solar collector. The SCPP can be modified into a giant photocatalytic methane removal system by integrating a PCR under the solar collector.

Some challenges of the technology were pointed out in the two latest reports (The Royal Society, 2018; IPCC, 2018) before it can be applied to a large scale. A broader assessment of its effectiveness is lacking. In this study, we evaluated the methane removal effectiveness of an SCPP-PCR system for the first time. Three-dimensional steady numerical
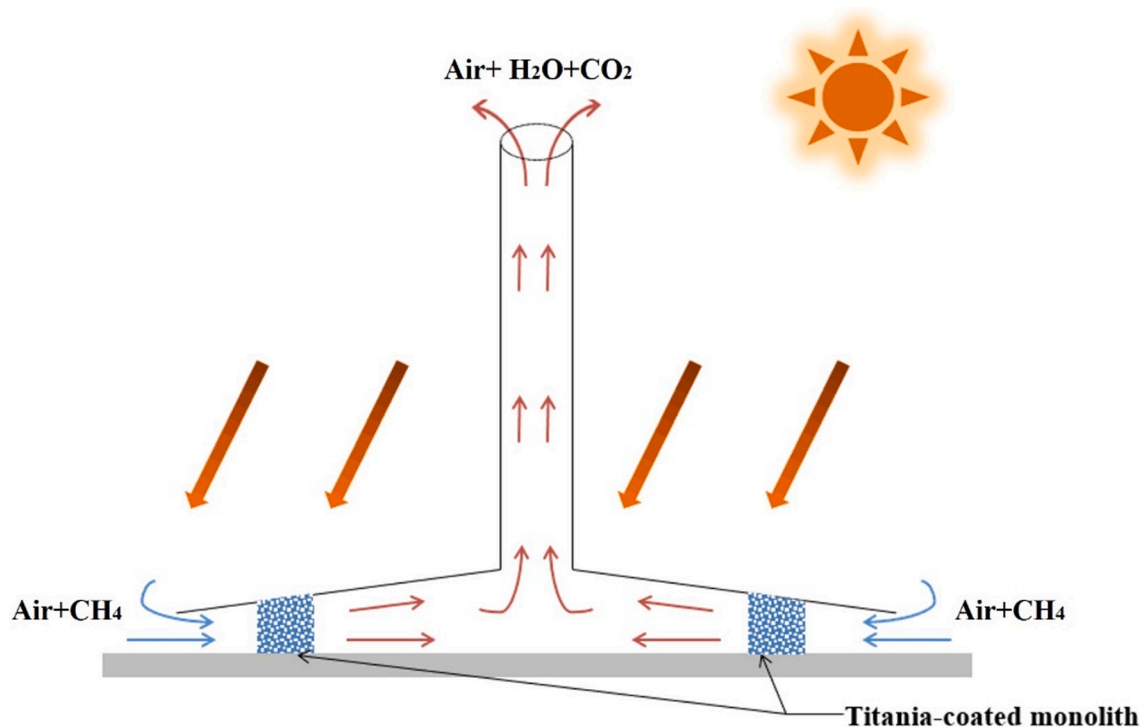
**Fig. 1.** Solar chimney power plant integrated with a photocatalytic reactor (SCPP-PCR) for atmospheric methane removal.

simulations of SCPP-PCR with the honeycomb monolith PCR of different pore diameters and channel lengths were carried out. The flow field characteristic and photocatalytic performance of the SCPP-PCR system were studied by analyzing the pressure, velocity and methane concentration distribution inside the system. Then, the effect of solar radiation intensitive on the degradation of atmospheric methane and the system flow performance under the optimum photoreactor dimension were discussed further. This timely work will help to guide the construction of an SCPP-PCR prototype and might provide a game-changing technology for atmospheric-scale methane removal.

## 2. Model description

### 2.1. Geometric model

A simplified model was adopted for the numerical analysis to investigate the performance of the SCPP-PCR to remove methane. As shown in Fig. 2, the model has a 200-m-high and 5-m-radial chimney with a 120-m radial collector. The collector has a slope in which the height increases from 2 to 6-m from the inlet to the center. As solar radiation is absorbed by the ground, the air inside the collector is continuously heated by the ground surface, resulting in a difference in air density between inside and outside of the system. Due to the stack effect, the air flows upward in the chimney at the center of the collector, and finally flows out of the chimney.

Many types of PCRs are available, such as the plate, tubular, and honeycomb PCRs (Rui, 2006; Hossain et al., 1999; Mo et al., 2008). Different PCR structures can have different specific surface areas, mass transfer rates, and photocatalytic reaction characteristics. The widely studied honeycomb monolith PCR (Fig. 3) has a large specific surface area and mass transfer rate. Therefore, this type of PCR was selected to be integrated with the SCPP system. Titanium dioxide (TiO$_2$) is an efficient, stable, cheap, and widely studied photocatalyst (Folli et al., 2010). It was selected to be coated on the internal channel surface of the honeycomb monolith PCR. The PCR was located 10-m away from the entrance to the collector. The direction of the honeycomb monolith
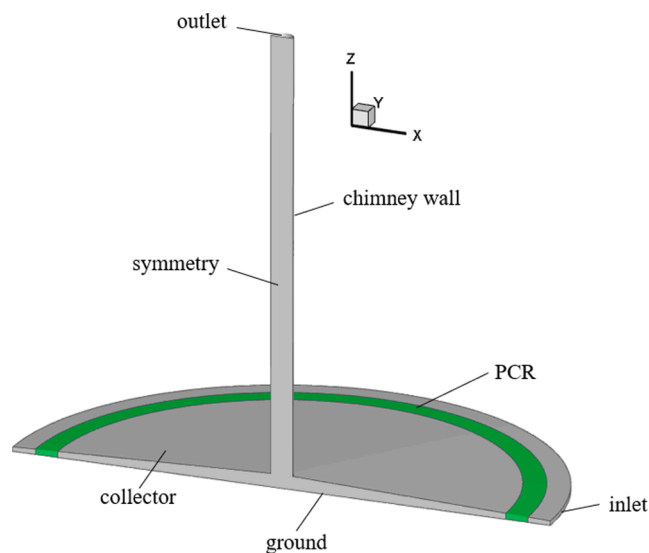


**Fig. 2.** Three-dimensional geometrical model of the solar chimney power plant integrated with a photocatalytic reactor (SCPP-PCR) system.

internal channels was along the path of airflow, ensuring the lowest pressure drop. The height of the PCR was the same as that of the collector, and the channel length of the honeycomb monolith was 3–10-m.

Because the SCPP-PCR model (as shown in Fig. 2) is symmetric in the XZ plane, only half of the model is used for the numerical simulation. This operation saves computing resources while maintaining the same calculation accuracy (Shen et al., 2014). The geometrical model does not consider the effects of the turbine or the energy storage layer. The main purpose of this study is to investigate the photocatalytic performance of the SCPP-PCR and analyze the flow characteristics of fluid in this system.
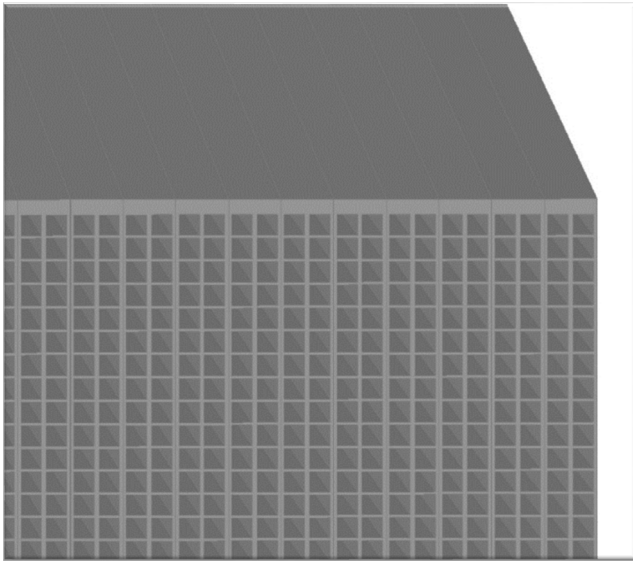
**Fig. 3.** Local enlarged image of honeycomb monolith photoreactor.

### 2.2. Mathematical model

The photocatalytic reaction zone was set as a porous zone and the remainder was set as the fluid zone. According to the flow characteristics of the system, the following assumptions were made:

(1) Solar heat radiation energy is steady.
(2) The sunlight or artificial light source can be guided to the photocatalytic reaction zone evenly by the side glow optical fibers, ensuring approximately 70% light intensity.
(3) Solar thermal radiation is distributed uniformly in the thermal storage layer.
(4) No homogeneous chemical reaction occurred.
(5) The thickness of the photocatalyst film on the surface of the porous zone is equal.
(6) The energy loss in the transition section between the chimney and the collector is not considered.

The airflow inside a conventional SCPP system is natural convection induced by solar radiation heating the ground surface. The Rayleigh number is a criterion number used to describe the strength of buoyancy-induced flow:

$$R_a = \frac{g\beta\Delta T H^3}{av} \tag{1}$$

where $g$ is gravitational acceleration, which is 9.81 m/s$^2$, $\beta$ is the thermal expansion coefficient, $\Delta T$ is the maximum temperature increase within the system, and $H$, $a$, and $v$ are the collector height, the thermal diffusivity, and the kinematic viscosity, respectively. The Rayleigh number value for the system was higher than $10^{10}$, indicating that fluid flow inside the system is in a vigorous turbulent state. Therefore, the turbulent mathematical model of standard k-$\varepsilon$ is selected to describe fluid flow within the system. In addition, the air density changes slightly in the entire calculation model. The error caused by ignoring air compressibility during simulation of a small-scale solar chimney power system, is less than 2% (Chen et al., 2013). Thus, the gas phase is assumed to be incompressible, and the ideal gas law is used to express the relationship between density and temperature for natural convection. As a result, the governing equations required for the entire simulation process include: the mass equation, the Navier–Stokes equation, the energy equation standard k-$\varepsilon$ equations, and the transport equations, which are written as follows:

Continuity equation:

$$\frac{\partial \rho}{\partial t} + \frac{\partial(\rho u_i)}{\partial x_i} = 0 \tag{2}$$

Navier–Stokes equation:

$$\frac{\partial(\rho u_i)}{\partial t} + \frac{\partial(\rho u_i u_j)}{\partial x} = \rho g_i - \frac{\partial p}{\partial x_i} + \frac{\partial \tau_{ij}}{\partial x_j} \tag{3}$$

Energy equation:

$$\frac{\partial(\rho c_p T)}{\partial t} + \frac{\partial(\rho c_p u_j T)}{\partial x_j} = \frac{\partial}{\partial x_j}\left(\lambda \frac{\partial T}{\partial x_j}\right) + \tau_{ij}\frac{\partial u_i}{\partial x_j} + \beta T\left(\frac{\partial p}{\partial t} + u_j \frac{\partial p}{\partial x_j}\right) \tag{4}$$

Equation for the turbulent kinetic energy $k$:

$$\frac{\partial(\rho k)}{\partial t} + \frac{\partial}{\partial x_i}(\rho k u_i) = \frac{\partial}{\partial x_j}\left(\alpha_k \mu_{eff} \frac{\partial k}{\partial x_j}\right) + G_k + G_b - \rho\varepsilon - Y_M + S_k \tag{5}$$

Equation for the energy dissipation:

$$\frac{\partial}{\partial t}(\rho\varepsilon) + \frac{\partial}{\partial x_i}(\rho\varepsilon u_i) = \frac{\partial}{\partial x_j}\left(\alpha_\varepsilon \mu_{eff}\frac{\partial\varepsilon}{\partial x_j}\right) + C_{1\varepsilon}\frac{\varepsilon}{k}(G_k + C_{3\varepsilon}G_b) - C_{2\varepsilon}\rho\frac{\varepsilon^2}{k} - R_\varepsilon + S_\varepsilon \tag{6}$$

Component transport equation:

$$\frac{\partial}{\partial t}(\rho Y_i) + \nabla\bullet(\rho\vec{v}Y_i) = -\nabla\bullet\vec{J_i} + R_i + S_i \tag{7}$$

where $\rho$, $t$, and $c_p$, represent the density, time, and constant-pressure specific heat; $G_k$ is the generation of turbulence kinetic energy because of the mean velocity gradients and is defined as $G_k = -\rho\overline{u_i' u_j'}\frac{\partial u_j}{\partial x_i}$, $\sigma_T, \sigma_k,$ and $\sigma_\varepsilon$ denote the turbulent Prandtl numbers for $T$, $k$, and $\varepsilon$ respectively: $\sigma_T = 0.9$, $\sigma_k = 1.0$, $\sigma_\varepsilon = 1.3$. $C_1$ and $C_2$ are two constants for the turbulent model: $C_{1\varepsilon}=1.44, C_{2\varepsilon} = 1.92$. $\vec{J_i}$ is the diffusion flux of species $i$: $\vec{J_i} = -\rho D_{i,m} + R_i$, $R_i$ is the net production rate of the chemical reaction, $S_i$ represents the extra rate due to the discrete phase, $Y_M$ represents the contribution of the fluctuating dilatation incompressible turbulence to the overall dissipation rate. To save computational resources, the reaction zone was set as the porous media model instead of introducing a large number of submicron scale meshes for simulation (Mazumder and Sengupta, 2002). The governing equations describing the inside of the porous media are:

Continuity equation:

$$\frac{\partial\gamma\rho}{\partial t} + \nabla\bullet(\gamma\rho\vec{v}) = 0 \tag{8}$$

Navier–Stokes equation:

$$\frac{\partial}{\partial t}(\gamma\rho\vec{v}) + \nabla\bullet(\gamma\rho\vec{v}\vec{v}) = -\gamma\nabla p(\gamma\overset{\text{\tiny$\backslash$}}{\tau}) + \gamma\rho\vec{g} + S_\Phi \tag{9}$$

where $\gamma$ is porosity of the porous medium, $\gamma= 0.85$. $\vec{v}$ and $p$ represent the velocity vector of the fluid and pressure, $\overset{\text{\tiny$\backslash$}}{\tau}$ represents the viscous stress tensor, $\overset{\text{\tiny$\backslash$}}{\tau} = \mu\left[\left(\nabla\vec{v} + \nabla\vec{v}^T - \frac{2}{3}\nabla\bullet\vec{v}I\right)\right]$. $S_\Phi$ denotes the momentum loss term: $S_\Phi = -\left(\frac{\mu}{K}\vec{v} + \frac{C_2}{2}\rho|\vec{v}|\vec{v}\right)$, where the first term on the right is the viscous loss term and the second term is the inertia loss term.

The honeycomb structure usually can be represented by a packed bed, and the permeability ($K$) and the inertia coefficient ($C$) in porous media are derived and calculated using the Ergun equation (Wang et al., 2014):

$$K = \frac{D_P^2}{150}\frac{\gamma^3}{(1-\gamma)^2} \tag{10}$$

$$C = \frac{3.5}{D_P} \frac{(1 - \gamma)}{\gamma^3} \tag{11}$$

where $D_P$ is the pore diameter of the porous media.

The specific surface area, *SSA,* of the honeycomb structure can be deduced (Wang et al., 2014):

$$SSA = \frac{(1 - \gamma)S}{V} = \frac{6(1 - \gamma)\pi D_P^2}{\pi D_P^3} = \frac{6(1 - \gamma)}{D_P} \tag{12}$$

where $S$ denotes the surface area of the porous media zone; $V$ represents the apparent volume of the porous media zone.

Andreas et al. (Haeger et al., 2004) deduced the surface reaction rate formula of total oxidation of methane by photocatalysis through oxygen-enriched experiments.

$$r_{AI} = B \frac{B_1 c_1}{1 + B_1 c_1} \frac{B_2 c_2}{1 + B_2 c_2} \tag{13}$$

where $r_{AI}$ represents the surface reaction rate of methane photocatalysis; $c_1$ is the concentration of methane; $c_2$ is the concentration of oxygen; and $B$, $B_1$, and $B_2$ are constants measured experimentally. The corresponding values of $B$, $B_1$, and $B_2$ are $5.37 \times 10^{-6}$, 2.42, and 4.60, respectively.

Overall, the actual photocatalytic rate $R_m$ in the honeycomb monolith photoreactor was calculated as follows:

$$R_m = SSA \times r_{AI} \tag{14}$$

### 2.3. Boundary conditions

The domain boundary conditions for computation of the SCPP-PCR are shown in Table. 1. Detailed descriptions of the boundary conditions are as follows. Relative static pressure was used for the simulation to analyze the entire pressure distribution of the system, which is the static pressure difference between the SCPP-PCR and the environment at the same height (Ming et al., 2010). The pressures at the entrance to the collector and the chimney outlet were set equal to the standard atmospheric pressure (101,325 Pa) when the height of the SCPP-PCR is relatively low (Gong et al., 2017). Namely, the relative static pressure of the collector inlet and chimney outlet was 0. The solar radiation heating the ground surface under the canopy was regarded as heat flux. The energy of absorption from the soil and the energy lost through thermal radiation and conduction were considered. Solar radiation was set to 857 W/m², and the corresponding heat flux on the ground surface was set to 600 W/m², according to typical solar radiation conditions in the deserts of northwest China (Ming et al., 2012). Assuming that the ambient air temperature is maintained at 293 K, convective heat transfer will occur on the canopy of the collector with the surrounding air, and it is acceptable for the coefficient of convection to be set to 10 W/(m²K) when air velocity is not very high (Xu et al., 2011).

### 2.4. Simulation method and validation

The computations were solved by the standard k-ε method and finite-rate reaction model in the general-purpose CFD program ANSYS Fluent 19.2. The numerical calculations were performed with the double precision solver. A simple algorithm was used for the pressure–velocity coupling scheme and the PRESTO! Discrete scheme was applied to discretize the pressure term. The standard wall functions method was used for the near wall region calculation. The QUICK scheme was employed in the discretization of the convective terms and the second-order upwind scheme was used for the discretization of the diffusion terms. Two ways were used to determine solution convergence. First, the maximum residuals of all variables were below $10^{-5}$. Second, the volume flow rate at the chimney outlet remained constant.

As a hexahedral (HEX) meshed grid system is more accurate and effectively avoids the influence of false diffusion on the computational results compared to tetrahedral grids, HEX grids were applied to discretize the computational region.

To validate the effectiveness of the numerical simulation in this study, the numerical results were compared with the Spanish prototype using the same parameters. Compared with the Spanish prototype experimental data (Haaf, 1984), the maximum temperature difference between the inlet and outlet of the system increased by 4.6% (the impact of ambient crosswind was neglected), but the velocity difference in the chimney was only 0.9%. As is shown in Table 2, the simulation results in this paper were in good agreement with the experimental results from the Spanish prototype. Obviously, this developed numerical model was able to predict the overall performance of SCPP-PCR system accurately.

Next, three test cases of the model were performed under the same conditions to determine if the numerical simulation results were grid independent. For the three different grid systems (the grid numbers were 1,646,307, 2,083,926, and 2,534,116 respectively), the corresponding volume flow rates at the chimney outlet were 885.08, 896.32, and 905.63 m³/s respectively. The less than 1.25% deviation demonstrates the grid-independence of simulations in this study. In general, the grid number of the basic mesh model in this paper was 2,083,926.

## 3. Results and discussion

As explained earlier, the ambient air surrounding the SCPP is continuously transported into the collector through the PCR. The photocatalytic oxidation of methane occurs inside the PCR as air passes through it. Then, the processed air with a lower methane concentration rises inside the chimney and is discharged to high altitude at the chimney exit.

The aim of this study is to investigate the effectiveness of the SCPP-PCR for degrading atmospheric methane and to test the flow performance of the system under different PCR dimensions. In the model, the honeycomb monolith PCR was placed inside the collector 10 m from the entrance to the collector. The PCR was treated as a porous medium. Porosity was 0.85. The pore diameter, $D_P$, of the PCR (i.e., channel diameter) varied from 2 to 4 mm at intervals of 0.5 mm, and the length $L$ of PCR (i.e., channel length) varied from 3 to 10 m at intervals of 1 m. Ambient air temperature, $T_0$, and solar irradiation intensity, $G$, were set to 293 K and 857 W/m², respectively.

### 3.1. Flow performance

Fig. 4 shows the contours of the static pressure distributions at the z = 1 m plane of the SCPP-PCR when $D_P$ of the PCR ranged from 2 to 4

**Table 1**
Boundary conditions.

| Location | Boundary type | Value |
|---|---|---|
| Collector inlet | Pressure inlet | p = 0 Pa, T = 293 K |
| Chimney outlet | Pressure outlet | p = 0 Pa |
| Ground surface | Heat flux | 600 W/m² |
| Collector canopy surface | convection | T = 293 K, h = 10 W/(m²K) |
| Chimney wall | Adiabatic wall | 0 W/m² |
| Symmetry surface | Symmetry | |

**Table 2**
Comparison of simulation results to the experimental data from the Spanish prototype.

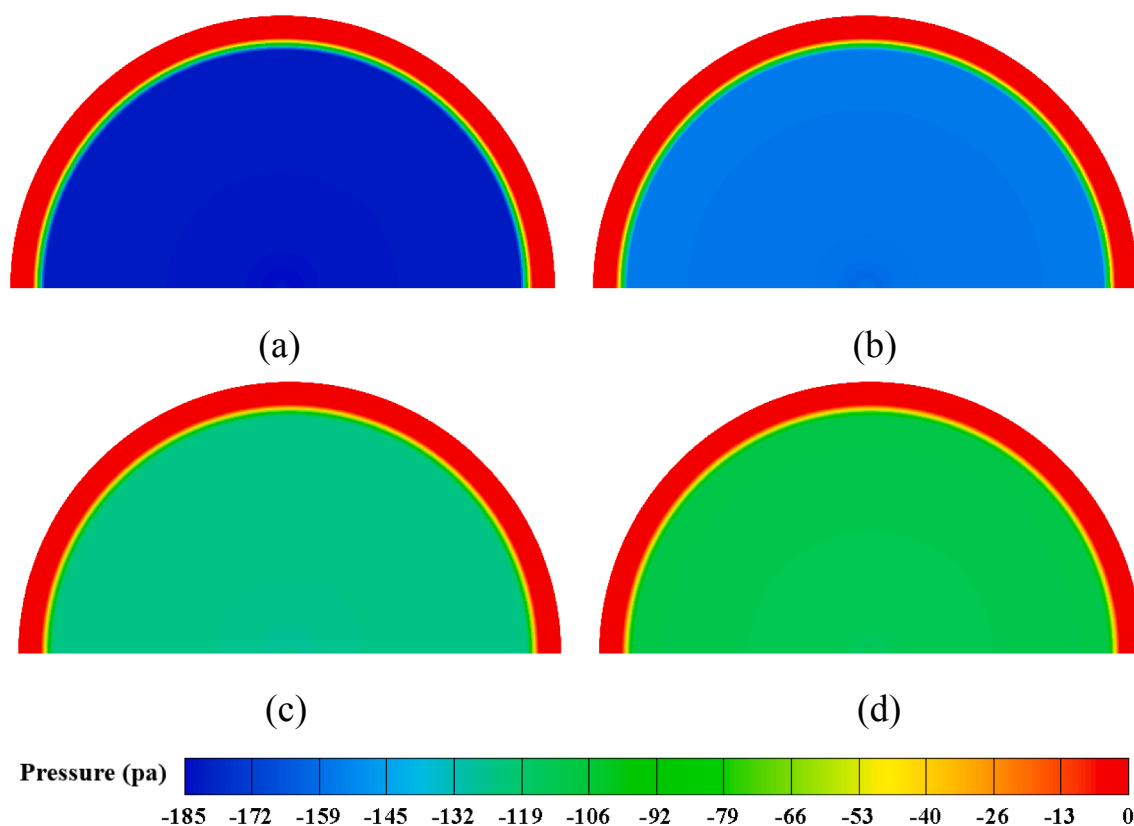| Parameters | Maximum temperature rise (K) | Chimney outlet velocity (m/s) |
|---|---|---|
| Experimental data | 17.5 | 9.10 |
| Calculated value | 18.3 | 9.18 |
| Tolerance | 4.6% | 0.9% |

**Fig. 4.** Effect of pore diameter on relative static pressure distributions in the z = 1 face at $L = 5$ m. (a)$D_P = 2$ mm, (b)$D_P = 2.5$ mm, (c)$D_P = 3.5$ mm, (d) $D_P = 4$ mm.

mm, and $L$ was 5 m. The pressure distribution before and after the PCR was uniform. When air flowed through the PCR of different pore diameters (i.e.$D_P = 2, 2.5, 3, 3.5,$ and 4 mm), it produced different pressure drops (i.e., 180.90, 155.70, 138.81, 124.03, and 110.52 Pa, respectively), as shown in Fig. 4(a–d). The pressure drop decreased as pore diameter increased. Namely, the energy loss caused by fluid flow inside the PCR decreased with pore diameter. The main reason for this phenomenon is that the porous media generates resistance to airflow. A smaller pore size causes more resistance and thus more energy loss and a greater pressure drop.

Fig. 5 shows a comparison of the contours of the velocity distributions at the symmetry plane (y = 0) under four different pore diameters. The patterns of velocity distribution in the system were similar. Airflow velocity was relatively slow under the collector but increased closer to the center of the chimney. As shown in Fig. 6a–d, the magnitude of the velocity in the system gradually increased with pore diameter.

The ground was heated by solar radiation, and heat converged into the chimney through convective heat transfer with the air under the collector. The updraft reached the maximum velocity at the bottom of the chimney from 10.26 to 11.86 m/s. The updraft velocity decreased gradually inside the chimney and then remained stable along the height. The average velocity at the chimney exit ranged from 7.70 to 8.93 m/s.

It can be concluded that the pore diameter of the PCR has a strong effect on flow performance, including the pressure drop and flow velocity. A smaller pore diameter produced a higher pressure drop and a slower flow velocity, while a larger pore diameter produced a lower pressure drop and a faster flow velocity.

We also investigated the effect of the other dimension (i.e., PCR length, $L$). Fig. 6 denotes the impact of PCR length on the pressure drop. The pressure drop in the PCR increased significantly as PCR length increased, regardless of the pore diameter, which can be explained similarly to that for pore diameter. The porous media generated resistance to airflow. A longer pore channel generated more wall friction and

more resistance and more energy lost with a higher pressure drop. The minimum pressure drop was about 80.45 Pa at$D_P = 4$ mm and$L = 3$ m, while the maximum pressure drop was 260.02 Pa at$D_P = 2$ mm and $L = 10$ m. The total energy loss from the SCPP system alone was mainly from the chimney outlet and the canopy of the collector (Gannon and Backström TWv, 2000). The weakening effect of the PCR on the natural convection intensity of the system cannot be ignored in a SCPP-PCR integrated system.

Fig. 7 shows the effects of a PCR (with different dimensions) on the velocity and the volume flow rate of the updraft from the chimney outlet. Updraft velocity almost decreased linearly with the increase in PCR length, and it increased with increasing pore diameter. Furthermore, the trend in the volume flow rate at the chimney outlet was consistent with the velocity. For example, when $L = 3$ m, the updraft velocity and volume flow rate decreased from 9.83 m/s and 772 m$^3$/s to 8.51 m/s and 668 m$^3$/s respectively, with pore diameters from 4 to 2 mm.

In summary, the pore diameter and length of the PCR have significant effects on flow performance, including the pressure drop, flow velocity, and volume flow rate. Shorter PCR lengths or a larger pore diameters produced less reduced convection intensity, such as less of a negative suction effect on the chimney.

### 3.2. Photocatalytic performance

Fig. 8 shows the methane concentration distribution inside the SCPP-PCR integrated system when the PCR was 5 m in length and with different pore diameters. The methane concentration at the entrance to the collector was 1,886 ppb, which was equal to that in the ambient atmosphere. Taking Fig. 8(a) as an example, due to photocatalytic oxidation of methane in the PCR, the methane concentration inside the collector began to decrease gradually at the entrance to the PCR and reached the minimum value at the PCR outlet. Then, air with a reduced
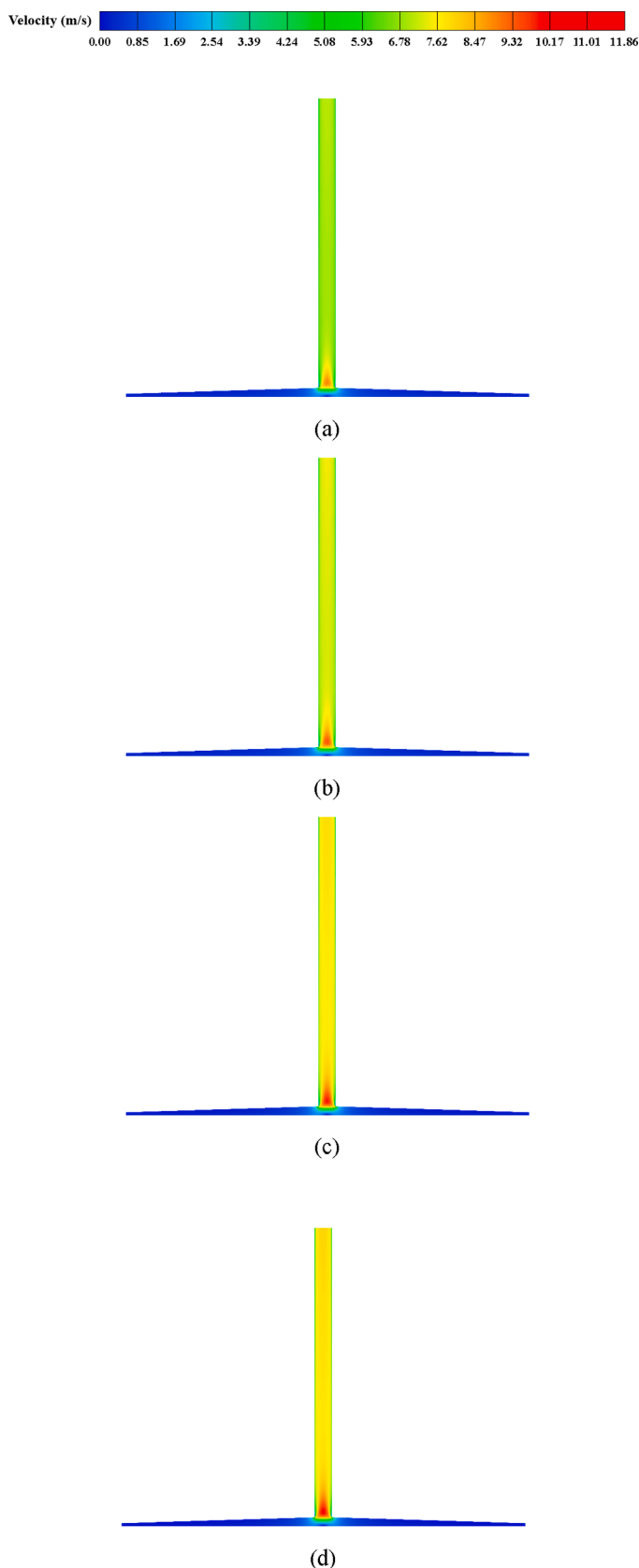
**Fig. 5.** Contours of velocity distribution in the y = 0 (symmetry) plane with the photoreactor length $L$ = 5 m. (a)$D_P$ = 2 mm, (b)$D_P$ = 2.5 mm, (c)$D_P$ = 3.5 mm, (d)$D_P$ = 4 mm.
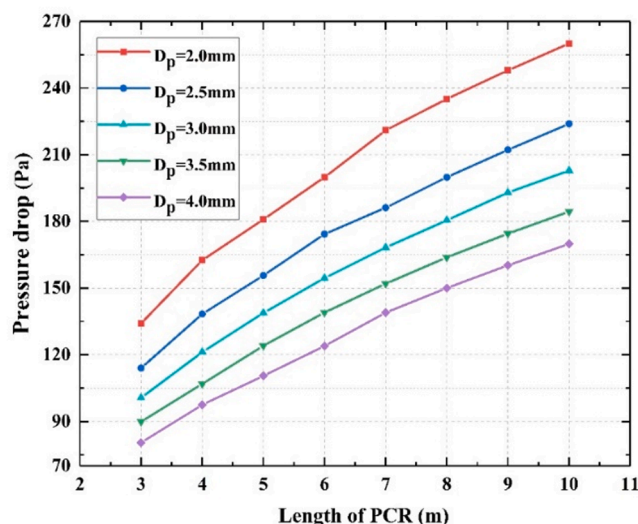


**Fig. 6.** Effect of PCR length on the pressure drop between the inlet and outlet of the PCR at $G$ = 857 W/m², $\gamma$ = 0.85.
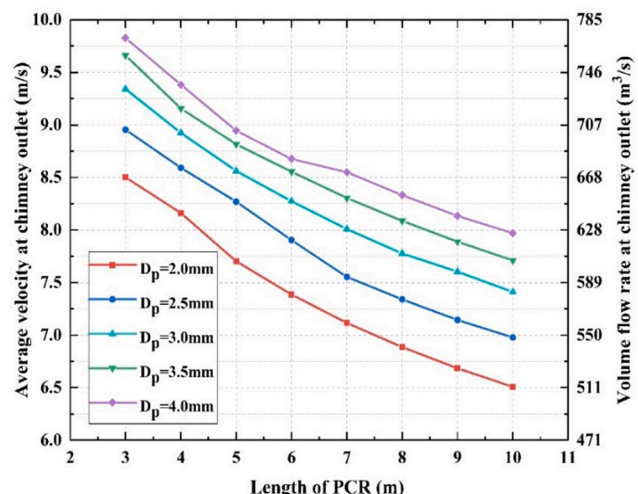


**Fig. 7.** Effect of PCR length on average velocity and volume flow rate at the chimney outlet. Under solar radiation of $G$ = 857 W/m², porosity of $\gamma$ = 0.85.

methane concentration flowed along the remainder of the collector to the bottom of the chimney due to natural convection. Fig. 8 (b) shows the same concentration distribution of methane at the symmetrical plane. The methane concentration inside the chimney remained evenly distributed. The methane concentration was 75 ppb at the chimney outlet. Namely, clean air with only 75 ppb methane was discharged back into the atmosphere.

The ratio of the methane concentration difference at the inlet and outlet of the system to inlet methane concentration was defined as photocatalytic efficiency $E_s$:

$$E_s = \frac{(J_1 - J_2)}{J_1} 100\% \tag{15}$$

where $J_1$ and $J_2$ are the methane concentrations at the entrance and exit of the system, respectively. The photocatalytic efficiency of the system in Fig. 8(a) and (b) was 96.02% when $L$ = 5 m and $D_P$ = 2 mm.

Fig. 8(c–f) shows the methane concentration distributions in the SCPP-PCR system with a larger PCR pore diameter. The patterns of distribution were similar to those in Fig. 8(a) and (b). The methane concentration at the chimney outlet was 219 ppb when $D_P$ = 3 mm. The
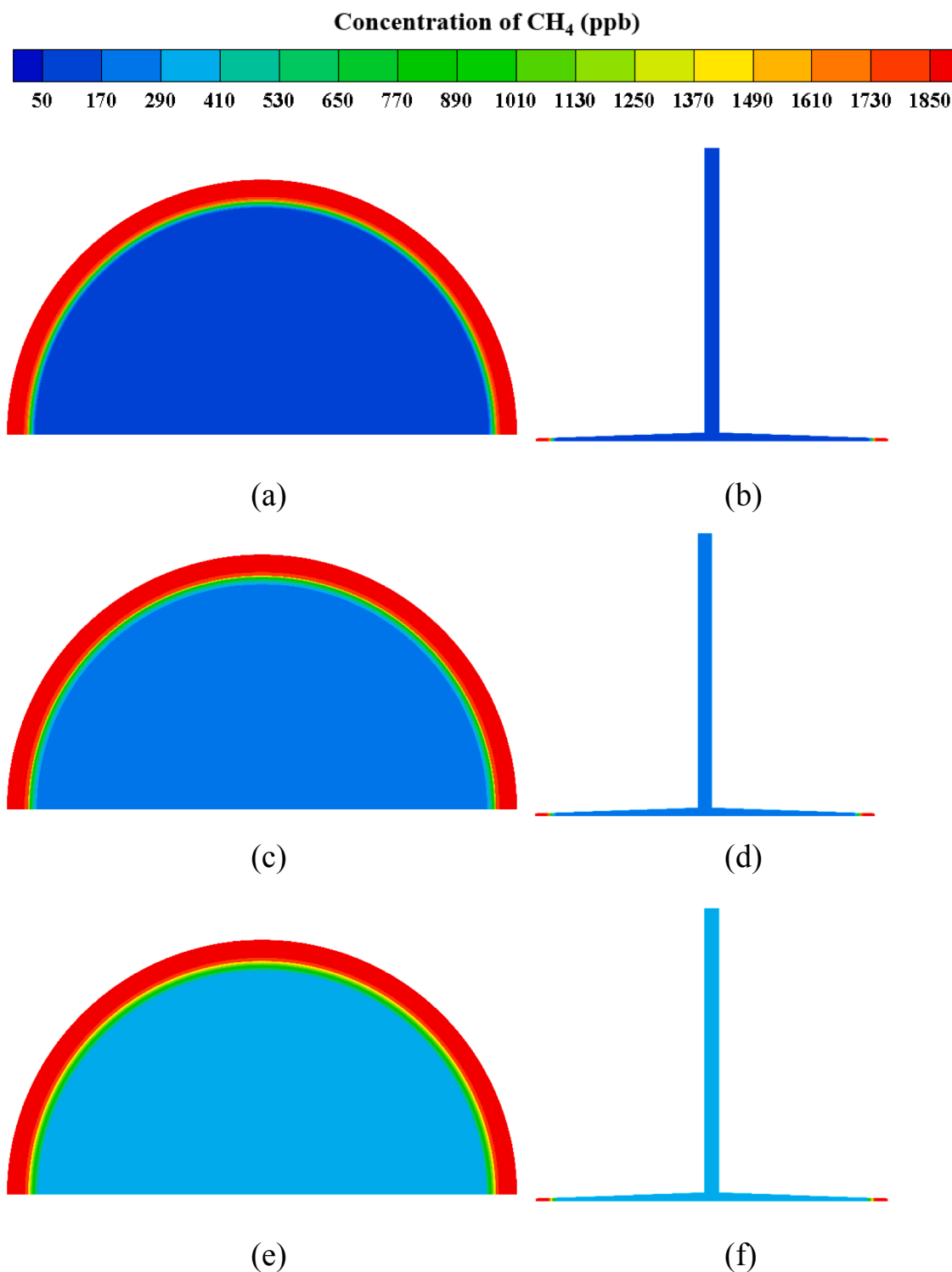
**Fig. 8.** Contours of the methane concentration distribution in the z = 1 m plane and y = 0 (the symmetry) plane with the photoreactor length $L = 5$ m. (a)$D_P = 2$ mm, z = 1, (b)$D_P = 2$ mm, y = 0 (c)$D_P = 3$ mm, z = 1 (d)$D_P = 3$ mm, y = 0, (e)$D_P = 4$ mm, z = 1, (f)$D_P = 4$ mm, y = 0. Under solar radiation of $G = 857$ W/m², porosity of $\gamma = 0.85$.

corresponding photocatalytic efficiency was 88.39%. The methane concentration at the chimney outlet was 375 ppb when$D_P = 4$ mm and the corresponding photocatalytic efficiency was 80.11%. Therefore, photocatalytic efficiency decreased with the pore diameter if the PCR length was the same.

Next, we investigated the effect of PCR length and pore diameter on photocatalytic performance. Fig. 9 shows the photocatalytic efficiency

of the system with different PCR dimensions. It is evident that with the increase of PCR length from 3 to 10 m, the photocatalytic efficiency of the system improved at all pore sizes. An increase in PCR length resulted in a larger reaction area and a longer reaction time inside. The increase in the photocatalytic efficiency was not linear. It increased rapidly when the PCR was lengthened from 3 to 4 m and became slower and gradually reached a plateau. This trend was clearer at smaller pore diameters.
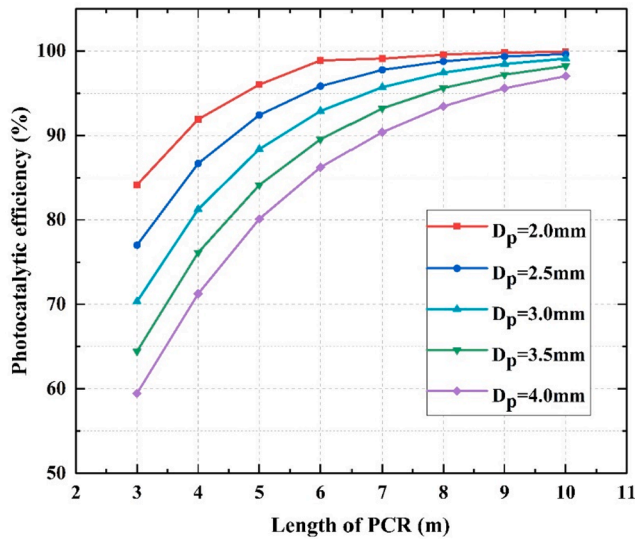
**Fig. 9.** Effect of PCR length on photocatalytic efficiency at $G = 857$ W/m$^2$, $\gamma$ = 0.85.

It was explained earlier that photocatalytic efficiency was different when pore diameter was changed at a given PCR length. Interestingly, the difference in photocatalytic efficiency caused by different pore diameters was smaller with a longer PCR. When the length of PCR was 10 m, all efficiency values were identical, with a difference of less than 5%. That is to say, when the length of the PCR increased to a certain extent, the change in pore diameter no longer played a crucial role in the catalytic efficiency of the system.

More importantly, the amount of methane removed by the SCPP-PCR system is more relevant to GHG removal effectiveness. Thus, we introduced a new evaluation index called the purification rate. The purification rate $R_p$ was defined as:

$$R_p = q_m \Delta z \tag{16}$$

where $\Delta z$ represents the difference of the mass fraction of CH$_4$ between the collector inlet and chimney outlet and $q_m$ is the air mass flow rate of the system flowing through the chimney outlet.

Fig. 10 shows the relationship between the purification rate of the SCPP-PCR system and the PCR dimensions. Considering $D_P = 3$ mm as an
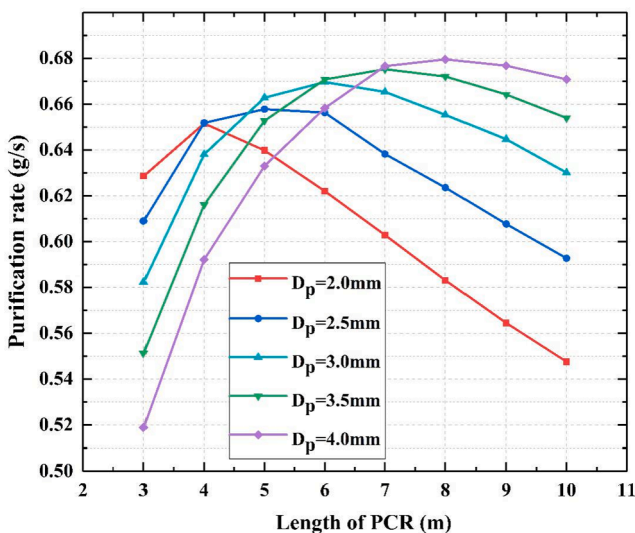
example, the purification rate climbed from a 3 m long PCR to a 6 m long PCR and then decreased with the increase in length of the PCR. These trends were similar for other pore diameters with different turning points. The influence of the PCR dimensions on the purification rate is a combination of flow rate (Fig. 7) and photocatalytic efficiency (Fig. 9). In the beginning, the length of the PCR was relatively short, and photocatalytic efficiency improved significantly when length was extended, while the loss of flow rate was not as significant as the improvement in photocatalytic efficiency. Therefore, the overall purification rate increased. When the length of the PCR was extended further, the gain in photocatalytic efficiency was less than the loss in flow rate, and the overall purification rate decreased.

As shown in Fig. 10, there was a maximum purification rate for each pore diameter. The peak values of $D_P = 2, 2.5, 3.0, 3.5,$ and 4.0 mm appeared respectively at $L = 4, 5, 6, 7,$ and 8 m. The overall optimum was 0.68 g/s of methane removal at $D_P = 4.0$ mm and $L = 8$ m.

### 3.3. Effects of solar radiation

To further discuss the effect of solar radiation on photocatalytic degradation of
atmospheric methane and the SCPP-PCR system flow performance, the solar radiation values of the Qianyanzhou area in Taihe County, Jiangxi Province, China on July 24, 2016 were adopted for the calculation (Bai, 2020), as shown in Table 2. The mean solar radiation value for every two adjacent hours was taken as an input data for the numerical model, namely, the solar radiation values for the 10 h from 7:00 a.m. to 5:00 p.m. were divided into five groups (i.e. 372, 776, 889, 808, and 507 W/m$^2$, respectively) (see Table 3).

Using $D_P = 4.0$ mm and $L = 8$ m as the PCR dimensions, and porosity was 0.85. Fig. 11 displays the changes in velocity and the volume flow rate of the updraft from the chimney outlet under different solar radiation levels. The updraft velocity and the volume flow rate increased with increasing solar radiation. Due to the lower solar irradiation from 7:00 a.m. to 9:00 a.m. and from 3:00 p.m. to 5:00 p.m., airflow inside the system was weaker than at other times of day. Greater solar irradiation generates stronger airflow in the SCPP-PCR system, and the solar irradiation remained relatively strong from 9:00 a.m. to 3:00 p.m. The maximum updraft velocity and volume flow rates were 8.38 m/s and 658 m$^3$/s, corresponding to 11 a.m. to 1 p.m.

Fig. 12 shows the photocatalytic efficiency and purification rate of the system under different solar radiation levels. Photocatalytic efficiency increased from 82.45% to 92.45% with the increase in solar radiation from 372 to 776 W/m$^2$, and photocatalytic efficiency increased by 10%. However, when solar radiation increased from 776 to 889 W/m$^2$, photocatalytic efficiency rose < 1.5%. It is evident that after solar radiation reached a specific value, the improvement in photocatalytic efficiency of the system may not be evident with increasing solar radiation. The trend was similar to the purification rate.

In fact, the increased solar radiation strengthened the natural convection to increase airflow and also increased light intensity in the PCR channel. The maximum photocatalytic efficiency and purification rates



**Fig. 10.** Effect of PCR length on the purification rate at $G = 857$ W/m$^2$, $\gamma$ = 0.85.

**Table 3**
Solar radiation data in the Qianyanzhou area, China.

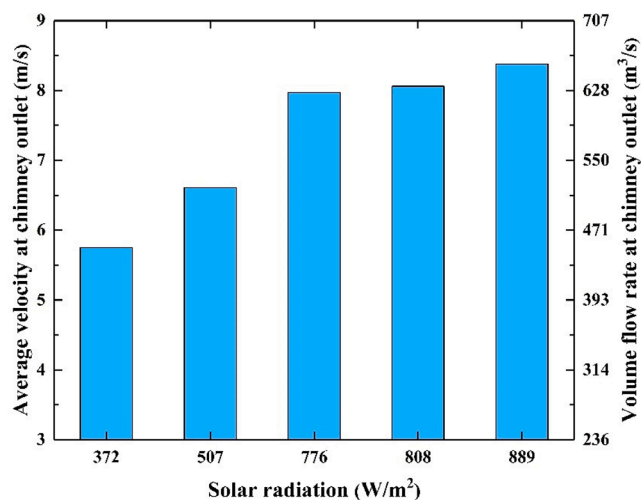| Time(Local Beijing time) (July 24, 2016) | Solar radiation (60 mins average) (W/m$^2$) | Time (Local Beijing time) (July 24, 2016) | Solar radiation (60 mins average) (W/m$^2$) |
|---|---|---|---|
| 7:00 am–8:00 am | 270 | 12:00 am–1:00 pm | 884.7 |
| 8:00 am–9:00 am | 474 | 1:00 pm–2:00 pm | 889.2 |
| 9:00 am–10:00 am | 715.3 | 2:00 pm–3:00 pm | 716.1 |
| 10:00 am–11:00 am | 837.5 | 3:00 pm–4:00 pm | 607.2 |
| 11:00 am–12:00 am | 892.8 | 4:00 pm–5:00 pm | 407.5 |

**Fig. 11.** Effect of solar radiation on average velocity and volume flow rate at the chimney outlet under $D_P = 4.0$ mm, $L = 8$ m and $\gamma = 0.85$.
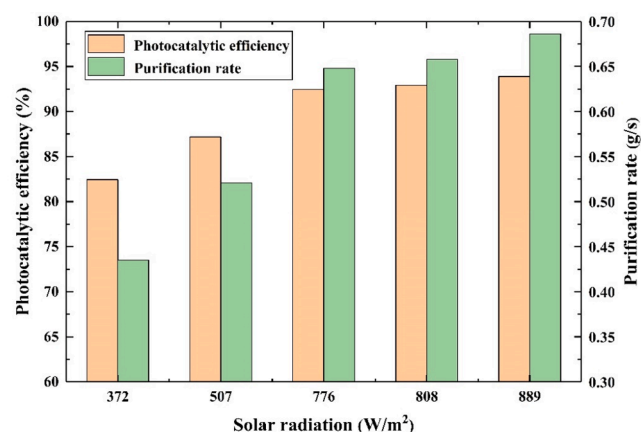


**Fig. 12.** Effect of solar radiation on photocatalytic efficiency and the purification rate under $D_P = 4.0$ mm, $L = 8$ m and $\gamma = 0.85$.

were 93.89% and 0.69 g/s, respectively, as shown in Fig. 12.

As shown in Figs. 11 and 12, according to the daily solar radiation conditions in the Qianyanzhou area (photocatalysis also occurs under intense sunlight for 10 h/day), the sum of the amount of methane removed by the SCPP-PCR system during these five time periods was calculated. Therefore, methane removal was calculated to be 21,312 g/day (nearly 21 kg/day).

The simulation results show that large-scale degradation of methane in the atmosphere by the SCPP-PCR integrated system is feasible. When the pore diameter of the honeycomb photoreactor was 4 mm, and length was 8 m, the SCPP-PCR system processed 21,312 g of atmospheric methane according to the actual solar radiation data for a particular day. Although the sunlight-driven photocatalysis in the system only operated 10 h or less per day, the turbine still produces electricity the rest of the time, and some strategies for night operation have been proposed, such as artificial illumination during the night or adding charcoal or biochar to the soil (Ming et al., 2016). The choice of dimensions or the type of PCR may also have an effect on the cost. In our further research, we will analyze an integrated system with a turbine to generate power.

## 4. Conclusions

In this study, we proposed a SCPP-PCR system to remove atmospheric-scale $CH_4$ and analyzed the flow properties and photocatalytic performance of the system under various PCR dimensions. The potential to remove $CH_4$ from the atmosphere was demonstrated through our numerical simulations. The approach is highly promising for solving the global warming problem. The numerical simulation results indicate that:

(1) The pore diameter and length of the PCR have the largest effects on flow performance, including pressure drop, flow velocity, and the volume flow rate. A shorter PCR or larger pore diameter produces a smaller pressure drop and a higher flow velocity and volume flow rate.
(2) The purification rate of the SCPP-PCR is determined by the system mass flow rate and the photocatalytic efficiency. The overall optimum was 0.68 g/s of methane removal at $D_P = 4.0$ mm and $L = 8$ m.
(3) The SCPP-PCR integrated system degraded 21,312 g methane per day under the solar radiation conditions of Qianyanzhou, China, when using a PCR with a pore diameter of 4 mm and length of 8 m.

## Declaration of Competing Interest

The authors declare that they have no known competing financial interests or personal relationships that could have appeared to influence the work reported in this paper.

## References

Bai, J., 2020. Dataset of surface solar radiation and meteorological elements at Qianyanzhouin, Taihe county, Jiangxi Province, China (2013–2016). National Tibetan Plateau Data Center.
Bernardes, M.A. dos S., Voß, A., Weinrebe, G., 2003. Thermal and technical analyses of solar chimneys. Sol. Energy 75 (6), 511–524.
Cao, Q., Kuehn, T.H., Lian, S., Chen, S.C., Zhang, N., Yu, H., et al., 2018. Urban-scale SALSCS, Part I: Experimental Evaluation and Numerical Modeling of a Demonstration Unit. Aerosol Air Qual. Res. 18.
Chen, Y.S., Chen, W.H., Pang, Y.J., 2013. The Impact Analysis of Air Compressibility in Solar Chimney Power Station. Appl. Mech. Mater. 283, 9–13.
Chen, X., Li, Y., Pan, X., Cortie, D., Huang, X., Yi, Z., 2016. Photocatalytic oxidation of methane over silver decorated zinc oxide nanocatalysts. Nat. Commun. 7, 12273.
Chen, H., Nanayakkara, C.E., Grassian, V.H., 2012. Titanium dioxide photocatalysis in atmospheric chemistry. Chem. Rev. 112 (11), 5919–5948.
de Richter, R.K., Ming, T., Caillol, S., 2013. Fighting global warming by photocatalytic reduction of CO2 using giant photocatalytic reactors. Renew. Sustain. Energy Rev. 19, 82–106.
de Richter, R., Ming, T., Davies, P., Liu, W., Caillol, S., 2017. Removal of non-CO2 greenhouse gases by large-scale atmospheric solar photocatalysis. Prog Energ Combust. 60, 68–96.
Folli, A., Pochard, I., Nonat, A., Jakobsen, U.H., Shepherd, A.M., Macphee, D.E., 2010. Engineering Photocatalytic Cements: Understanding TiO2 Surface Chemistry to Control and Modulate Photocatalytic Performances. J. Am. Ceram. Soc. 93 (10), 3360–3369.
Gallus, M., Ciuraru, R., Mothes, F., Akylas, V., Barmpas, F., Beeldens, A., Bernard, F., Boonen, E., Boréave, A., Cazaunau, M., Charbonnel, N., Chen, H., Daële, V., Dupart, Y., Gaimoz, C., Grosselin, B., Herrmann, H., Ifang, S., Kurtenbach, R., Maille, M., Marjanovic, I., Michoud, V., Mellouki, A., Miet, K., Moussiopoulos, N., Poulain, L., Zapf, P., George, C., Doussin, J.F., Kleffmann, J., 2015. Photocatalytic abatement results from a model street canyon. Environ Sci Pollut R. 22 (22), 18185–18196.
Gannon, A.J., Backström, T.W.V., 2000. Solar Chimney Cycle Analysis With System Loss and Solar Collector Performance. J. Sol. Energ.-T. ASME. 122 (3), 133–137.

Gong, T., Ming, T., Huang, X., de Richter, R.K., Wu, Y., Liu, W., 2017. Numerical analysis on a solar chimney with an inverted U-type cooling tower to mitigate urban air pollution. Sol. Energy 147, 68–82.

Guerrini, G.L., 2012. Photocatalytic performances in a city tunnel in Rome: NOx monitoring results. Constr. Build. Mater. 27 (1), 165–175.

Guo, P., Li, J., Wang, Y., Wang, Y., 2016. Evaluation of the optimal turbine pressure drop ratio for a solar chimney power plant. Energy Convers. Manage. 108, 14–22.

Guo, P., Li, T., Xu, B., Xu, X., Li, J., 2019. Questions and current understanding about solar chimney power plant: A review. Energy Convers. Manage. 182, 21–33.

Haaf, W., 1984. Solar tower, part ii: Preliminary test results from the manzanares pilot plant. Sol. Energy 2, 41–61.

Haaf, W., Friedrich, K., Mayr, G., Schlaich, J., 1983. Solar Chimneys Part I: Principle and Construction of the Pilot Plant in Manzanares. Int. J. Solar Energy. 2 (1), 3–20.

Haeger, A., Kleinschmidt, O., Hesse, D., 2004. Photocatalytic Gas Reactions Using Titanium Dioxide as the Catalyst Part II: Photocatalyzed Total Oxidation of Alkanes with Oxygen. Chem. Eng. Technol. 27 (9), 1019–1026.

Hossain, M.M., Raupp, G.B., Hay, S.O., Obee, T.N., 1999. Three-Dimensional Developing Flow Model for Photocatalytic Monolith Reactors. AIChE J. 45 (6), 1309–1321.

In, S.-i., Nielsen, M.G., Vesborg, P.C.K., Hou, Y., Abrams, B.L., Henriksen, T.R., Hansen, O., Chorkendorff, I.b., 2011. Photocatalytic methane decomposition over vertically aligned transparent TiO2 nanotube arrays. Chem. Commun. 47 (9), 2613. https://doi.org/10.1039/c0cc02570d.

Special Report: Global Warming of 1.5 °C, 2018. Intergovernmental Panel on Climate Change (IPCC).

Jackson, R.B., Solomon, E.I., Canadell, J.G., Cargnello, M., Field, C.B., 2019. Methane removal and atmospheric restoration. Nat. Sustain. 2.

Kasaeian, A.B., Molana, S.h., Rahmani, K., Wen, D., 2017. A review on solar chimney systems. Renew. Sustain. Energy Rev. 67, 954–987.

Krishna, V., Kamble, V.S., Selvam, P., Gupta, N.M., 2004. Sunlight-Assisted Photocatalytic Oxidation of Methane over Uranyl-Anchored MCM-41. Catal. Lett. 98 (2-3), 113–116.

Li, X., Yu, J., Jaroniec, M., Chen, X., 2019. Cocatalysts for Selective Photoreduction of CO2 into Solar Fuels. Chem. Rev. 119 (6), 3962–4179.

Liu, Y., Ming, T., Wu, Y., de Richter, R., Fang, Y., Zhou, N., 2020. Desalination of seawater by spray freezing in a natural draft tower. Desalination 496, 114700. https://doi.org/10.1016/j.desal.2020.114700.

Maia, C.B., Ferreira, A.G., Valle, R.M., Cortez, M.F.B., 2009. Theoretical evaluation of the influence of geometric parameters and materials on the behavior of the airflow in a solar chimney. Comput. Fluids 38 (3), 625–636.

Mazumder, S., Sengupta, D., 2002. Sub-grid scale modeling of heterogeneous chemical reactions and transport in full-scale catalytic converters. Combust. Flame 131 (1-2), 85–97.

Ming, Tingzhen, de Richter, Renaud, Shen, Sheng, Caillol, Sylvain, 2016. Fighting global warming by greenhouse gas removal: destroying atmospheric nitrous oxide thanks to synergies between two breakthrough technologies. Environ. Sci. Pollut. R. 23 (7), 6119–6138.

Ming, T., Liu, W., Xu, G., 2010. Analytical and numerical investigation of the solar chimney power plant systems. Int J Energ Res. 30, 861–873.

Ming, T., Wang, X., de Richter, R.K., Liu, W., Wu, T., Pan, Y., 2012. Numerical analysis on the influence of ambient crosswind on the performance of solar updraft power plant system. Renew. Sustain. Energy Rev. 16 (8), 5567–5583.

Ming, T., de Richter, R.K., Meng, F., Pan, Y., Liu, W., 2013. Chimney shape numerical study for solar chimney power generating systems. Int J Energ Res 37 (4), 310–322.

Ming, T., Liu, W., Caillol, S., 2014. Fighting global warming by climate engineering: Is the Earth radiation management and the solar radiation management any option for fighting climate change? Renew. Sustain. Energy Rev. 31, 792–834.

Ming, T., Gong, T., de Richter, R., Liu, W., Koonsrisuk, A., 2016. Freshwater generation from a solar chimney power plant. Energy Convers. Manage. 113 (1), 189–200.

Ming, T., Wu, Y., de Richter, R.K., Liu, W., Sherif, S.A., 2017. Solar updraft power plant system: A brief review and a case study on a new system with radial partition walls in its collector. Renew. Sustain. Energy Rev. 69, 472–487.

Mo, J., Zhang, Y., Yang, R., Xu, Q., 2008. Influence of fins on formaldehyde removal in annular photocatalytic reactors. Build. Environ. 43 (3), 238–245.

Mohamedali, M., Ayodele, O., Ibrahim, H., 2020. Challenges and prospects for the photocatalytic liquefaction of methane into oxygenated hydrocarbons. Renew. Sustain. Energy Rev. 131, 110024. https://doi.org/10.1016/j.rser.2020.110024.

Rui, Y., 2006. A new method for measuring the reaction coefficients of a photocatalyst. J. Eng. Thermophys.-Rus. 41, 1221–1229.

Shen, W., Ming, T., Ding, Y., Wu, Y., de Richter, R.K., 2014. Numerical analysis on an industrial-scaled solar updraft power plant system with ambient crosswind. Renew. Energ. 68, 662–676.

Greenhouse gas removal, 2018. The Royal Society.

Wang, X., Tan, X., Yu, T., 2014. Modeling of Formaldehyde Photocatalytic Degradation in a Honeycomb Monolith Reactor Using Computational Fluid Dynamics. Ind. Eng. Chem. Res. 53 (48), 18402–18410.

Wu, Y., Ming, T., de Richter, R., Höffer, R., Niemann, H.-J., 2020. Large-scale freshwater generation from the humid air using the modified solar chimney. Renew Energ. 146, 1325–1336.

Xiang, Q., Yu, J., Jaroniec, M., 2012. Graphene-based semiconductor photocatalysts. Chem. Soc. Rev. 41 (2), 782–796.

Xu, G., Ming, T., Pan, Y., Meng, F., Zhou, C., 2011. Numerical analysis on the performance of solar chimney power plant system. Energy Convers. Manage. 52 (2), 876–883.

Yuliati, L., Yoshida, H., 2008. Photocatalytic conversion of methane. Chem. Soc. Rev. 37 (8), 1592. https://doi.org/10.1039/b710575b.

Zhou, X., Xu, Y., Yuan, S., Wu, C., Zhang, H., 2015. Performance and potential of solar updraft tower used as an effective measure to alleviate Chinese urban haze problem. Renew. Sustain. Energy Rev. 51, 1499–1508.

Zhou, X., Xu, Y., 2016. Solar updraft tower power generation. Sol. Energy 128, 95–125.

Zhou, X., Yang, J., Xiao, B.o., Shi, X., 2008. Special Climate around a Commercial Solar Chimney Power Plant. J Energ Eng. 134 (1), 6–14.

Zuo, L.u., Ding, L., Chen, J., Liu, Z., Qu, N., Zhou, X., Yuan, Y., 2018. The effect of different structural parameters on wind supercharged solar chimney power plant combined with seawater desalination. Energy Convers. Manage. 176, 372–383.